Corrosion Severity Index (CSI) for Spectral Characterization of Corroded Steel and Iron Samples

Emma Hernández-Suárez⬦, Adrián Rodríguez-Molina⬦, Ámbar Pérez-García⬦, *Student Member, IEEE*, Julia Mirza-Rosca⬦, and José López⬦

Abstract— Metals in coastal regions are threatened by corrosion, underscoring the need for precise detection and monitoring methods. Traditional methods often face limitations in terms of accuracy and applicability under diverse conditions. This study introduces the corrosion severity index (CSI), an innovative spectral index for assessing corrosion in steel and iron structures. Several iron samples were placed in a salt spray chamber to generate different degrees of corrosion. The samples were analyzed using hyperspectral cameras covering the visible near-infrared (VNIR) to the shortwave infrared (SWIR) spectrum. A scale-invariant feature transform (SIFT) registration algorithm was employed to generate the full spectral signatures from 400 to 1700 nm for each pixel. The CSI combines four spectral bands (457.50, 791.91, 1305.08, and 1442.60 nm) where a pixel value close to 0 represents the absence of corrosion, whereas a higher value indicates greater severity of corrosion. Based on the average CSI values, samples are classified into Grade A, B, C, or D, which indicates the degree of corrosion. CSI demonstrates its ability to detect early-stage corrosion and has been evaluated for robustness across a variety of steel and iron samples in different environmental conditions. In addition, the performance of the CSI is validated by comparing it with the previously published corrosion index (CI). CSI demonstrates a higher accurate ability to detect corrosion products and identify the degree of corrosion with a simplified approach. This index allows a balance between accuracy, low computational demands, and usability, providing an optimal solution for early diagnosis and proactive management of corrosion in coastal infrastructures.

Index Terms— Corrosion, early-stage corrosion, hyperspectral imaging (HSI), multispectral camera, spectral indices.

I. INTRODUCTION

THE coastal environment is significantly impacted by corrosion, an inevitable consequence of metals in constant exposure to the salinity of seawater and other corrosive agents [1], [2], [3]. This phenomenon compromises the functionality and safety of various steel and iron structures and artifacts, such as offshore platforms [4], ships [5], or bridges [6]. Effective corrosion monitoring and prediction are essential not only for ensuring the safety and integrity of these structures but also for enhancing operational efficiency, achieving cost savings, and protecting the environment [7].

Several nondestructive techniques (NDT) have been developed to automate corrosion detection without damaging the material [8]. Traditional methods such as linear polarization resistance (LPR) [9], ultrasonic testing (UT) [10], [11], eddy current [12], electrical resistance (ER) [13], and electrochemical impedance spectroscopy (EIS) [14], [15], [16] play a critical role in identifying corrosion. These techniques are often referred to as direct methods because they assess corrosion based directly on the physical or chemical effects that corrosion produces in the material [17]. However, they have significant limitations. The requirement for direct contact with the material limits their applicability for inspecting large surfaces or hard-to-reach areas. In addition, these methods may find difficulties in detecting early stage or under thin coatings challenging, where initial signs are minimal.

In contrast, indirect methods are based on parameters that indirectly influence the corrosion process, such as temperature, molecular structure, texture, or surface color. These methods include chemical analysis techniques such as the Fourier transform infrared (FTIR) spectroscopy [18], [19], [20], the Raman spectroscopy [21], and the X-ray spectroscopy [22], which use the spectral properties of materials to obtain information about their composition and structure. Although these methods allow noncontact and accurate detection of corrosion, their range is generally confined to small areas, and in certain scenarios, their implementation in field operations can be challenging [23].

Instead, optical techniques include RGB, multispectral, and hyperspectral sensors. Methods using RGB sensors measure the intensity of the primary colors (red, green, blue) and are mainly focused on the intensity, color, and texture

characteristics of the metal. This method is simple and uses collected information that is usually processed by machine learning (ML) and deep learning (DL) algorithms to detect and quantify corrosion [24], [25], [26], [27]. However, these algorithms generate a large number of false positives by misidentifying colors or textures similar to corrosion [28]. Furthermore, they do not facilitate early detection of this phenomenon, as their analysis is limited to what is visually observable.

Unlike RGB sensors, which are limited to three spectral channels, multispectral and hyperspectral sensors provide more detailed analysis by providing a high number of spectral bands. Specifically, hyperspectral sensors have the ability to scan a wide range of the electromagnetic spectrum, spanning the visible near-infrared (VNIR) spectra, as well as the short-wave infrared (SWIR). This amount of information enables the production of images in which each pixel reflects a unique spectral signature, allowing the precise identification of the composition of surfaces and revealing details not visible to the naked eye. In contrast, multispectral sensors capture images in a narrower, yet specific, range of the electromagnetic spectrum, typically between four and ten bands. Although they provide less information than hyperspectral sensors, multispectral sensors offer simplified image acquisition through instantaneous capture (snapshot). This is in stark contrast to the linear scanning (push broom) approach common to hyperspectral imaging (HSI) [29], [30].

Multispectral and hyperspectral technology offers a balance, allowing the analysis of large or small areas, without the need for direct contact, and without compromising accuracy. Although these techniques cannot probe under coatings, a detailed surface examination can reveal much about the underlying condition of the material.

Multispectral and hyperspectral imaging, originally developed for remote sensing purposes [31], [32], [33], has found wide-ranging applications across diverse fields, including medicine [34], [35], food safety and quality [30], [36], and precision agriculture [37], [38]. The corrosion domain has benefited significantly from these technologies in recent years. The breakthrough came in 2016 when Simova and Rochefort [39] highlighted the potential of multispectral imaging in the identification of different materials and corrosion types. Subsequently, Rowley's thesis [40] and the study by Lavadiya et al. [28] have demonstrated the superiority in terms of accuracy of hyperspectral imaging over traditional RGB imaging in corrosion detection. This technique has been successfully applied in the analysis of corrosion on outdoor bronze sculptures [41] and in the development of hyperspectral imaging probes designed for inspections in dark and difficult-to-access areas [42], [43]. Advances by De Kerf et al. [44] in determining corrosion levels in carbon steel have demonstrated the precise ability of these technologies to differentiate between corrosion stages. In addition, molecular structure studies have facilitated the identification of specific corrosion products, allowing accurate assessment of steel condition [44], [45]. Finally, chloride ion (Cl-) concentration has emerged as a key indicator for corrosion detection in steel reinforcing bars [46].

These studies have largely employed ML and DL algorithms, which have proven to be useful tools for analyzing and processing data obtained from hyperspectral images. These algorithms facilitate the identification and classification of corrosion patterns although the efficiency of these methods also depends on the quality and quantity of the trained dataset.

Spectral indices are one of the most widely used approaches to multispectral and hyperspectral data management. A spectral index is a numerical value derived from mathematical operations performed on different bands of the electromagnetic spectrum used to highlight specific characteristics of a surface or object [47], [48]. These measures identify, characterize, and quantify features such as vegetation quality [49], [50], [51], soil moisture [52], or oil spills [53]. Spectral indices offer advantages in terms of lower computational costs compared to ML and DL algorithms and do not require an extensive database for training. However, in certain applications, the limitations of spectral indices compared to ML and DL algorithms could be a challenge in terms of versatility. In the field of corrosion, the application of spectral indices has not been as widespread due to the complexity of the diversity of corrosion products and different types of steel. Zabalza et al. [54] developed a spectral index specifically aimed at this problem, the corrosion index (CI). Designed to evaluate corrosion in nuclear packages and focused on two types of steel (365L and 2205), the results of this index have been satisfactory and represent a promising advance. CI evaluates the spectral response obtained against a reference, corresponding to the spectral signature of an advanced corrosion state for the type of steel analyzed. This comparison quantifies the differences using the angular cosine distance (ACD) [55]. Subsequently, to refine this evaluation, the ACD values are adjusted using calibration parameters, empirically determined for each type of steel.

Corrosion represents a major challenge, especially in coastal environments where atmospheric conditions accelerate the deterioration of steel and iron structures. Accurate detection of affected areas is essential to implement effective maintenance measures, extend the lifespan of infrastructures, reduce costs, and ensure their functionality and safety. Although various noninvasive techniques have advanced corrosion monitoring, there is still a need for a method that combines accuracy, simplicity, processing speed, and low computational demand. In this context, the corrosion severity index (CSI) introduced by the authors emerges as an innovative tool designed to accurately and reliably assess the degree of corrosion of steel and iron. This index stands out for its simple approach that requires only four spectral bands, facilitating its use in multispectral cameras. The study methodology involves preparing iron samples, exposing them to different levels of corrosion in a salt spray chamber, and capturing images with hyperspectral cameras spanning the VNIR and SWIR ranges. A registration algorithm processes these images to obtain a complete spectral signature. The CSI demonstrates its ability to detect corrosion in its early stages and its robustness by successfully identifying corrosion in different steel and iron types. Validation is performed by comparison with the CI index, showing improved accuracy regarding the diversity of corrosion products and providing a more detailed analysis

Fig. 1. Experimental setup for the salt spray chamber.

TABLE I
SUMMARY OF SSC SAMPLES

SSC Samples	Level	Exposure time (h)
Samples 1, 2, 3	Level 0	0
Samples 4, 5, 6	Level 1	1/2
Samples 7, 8, 9	Level 2	1
Samples 10, 11, 12	Level 3	24

of the corrosion degree. This research not only contributes to the field of corrosion monitoring with a revolutionary tool but also establishes a solid foundation for future practical applications.

II. MATERIALS AND METHODS

A. Steel and Iron Samples' Preparation

For this study, two datasets have been developed. The first dataset, known as Salt Spray Chamber Samples (SSC Samples), was designed to corrode the plates in a controlled environment, allowing for validation of the spectral index. In contrast, the second dataset, Outdoor Conditions Samples (OC Samples), incorporates a variety of environmental conditions to assess the robustness and adaptability of the index under different real-world scenarios.

In order to obtain SSC Samples, 12 plates with iron (99.60% purity) were procured. The purity was obtained through initial characterization using an Oxford Instruments X-MET7000 Series fluorescence spectrometer [56]. These samples, measuring 100×100 mm, were subjected to a sandblasting process to eliminate any corrosion or surface imperfections. Samples 1, 2, and 3 were kept corrosion-free and designated as Level 0 samples. The remaining nine plates were exposed to 35 °C temperature and 5% NaCl solution in a salt spray chamber (see Fig. 1). Table I provides a summary of the iron samples and their exposure time in the salt spray chamber. Samples 4, 5, and 6 (Level 1) were subjected to 30 min of exposure; Samples 7, 8, and 9 (Level 2) were exposed for 1 h; and Samples 10, 11, and 12 (Level 3) were exposed for 24 h. Fig. 2 shows the RGB images after this process.
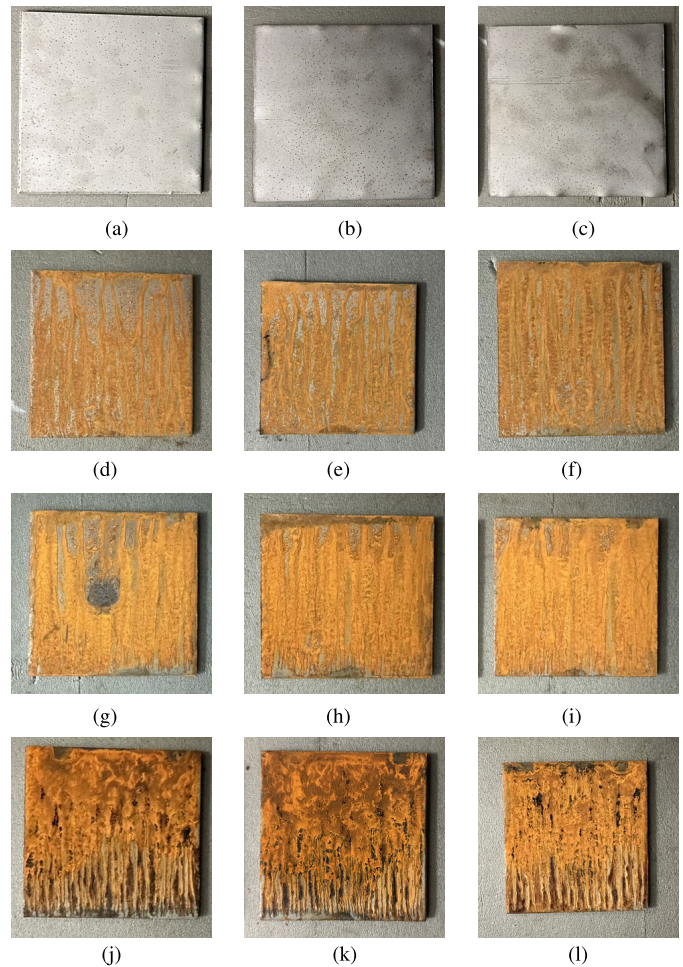

Fig. 2. RGB images of SSC Samples. (a) Sample 1. (b) Sample 2. (c) Sample 3. (d) Sample 4. (e) Sample 5. (f) Sample 6. (g) Sample 7. (h) Sample 8. (i) Sample 9. (j) Sample 10. (k) Sample 11. (l) Sample 12.

TABLE II
CHARACTERISTICS OF OC SAMPLES

OC Samples	Type of metal	Height x Width (mm)
Samples 1	Iron (99.40% purity)	150x150
Samples 2	Iron (99.40% purity)	150x150
Samples 3	Steel C-1020 [59]	180x80
Samples 4	Steel S355 [60]	150x75

Meanwhile, the OC Samples dataset comprises various types of steel and iron plates subjected to varying treatments and exposed to outdoor conditions. Table II displays the metal plates used, along with their respective metal type and dimensions.

Each plate was subjected to an initial sandblasting treatment. Following this, Samples 1, 2, and 3 were exposed to outdoor conditions for a duration of two weeks. Sample 1 did not receive any further treatment. For Sample 2 and Sample 3, seawater was poured daily into one half, whereas the other half was shielded with a protective cover. To document the changes over time, images were captured on a weekly schedule, that is, on days 0, 7, and 14 (see Fig. 3).

In addition, Sample 3 was subjected to hyperspectral imaging before the sandblasting treatment to study the behavior of the spectral index in the presence of mill scale; a layer
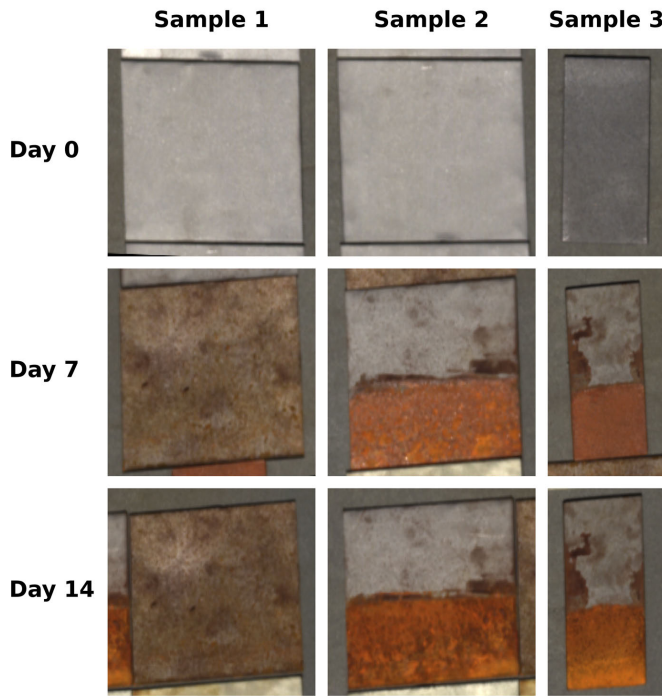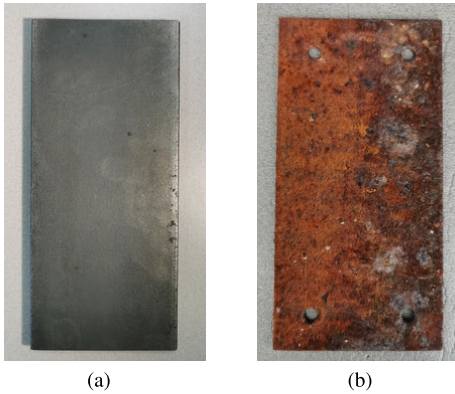
Sample 1 **Sample 2** **Sample 3**

Fig. 3.   RGB images of OC Samples.

(a)   (b)

Fig. 4.   RGB images of OC Samples. (a) Sample 3 m. (b) Sample 4.

TABLE III
GRADES OF SSC SAMPLES

SSC Samples	Level	Grade
Samples 1, 2, 3	Level 0	Grade A
Samples 4, 5, 6	Level 1	Grade B
Samples 7, 8, 9	Level 2	Grade B
Samples 10, 11, 12	Level 3	Grade C

TABLE IV
GRADES OF OC SAMPLES

OC Samples	Day	Grade
	Day 0	Grade A
Samples 1	Day 7	Grade B
	Day 14	Grade B
	Day 0	Grade A
Samples 2	Day 7	Grade B
	Day 14	Grade B
	Day 0	Grade A
Samples 3	Day 7	Grade B
	Day 14	Grade B
Samples 3m	-	Grade A
Samples 4	Day 210 (four months)	Grade D

TABLE V
SPECIM FX10 AND FX17 MAIN CHARACTERISTICS

	FX10	FX17
Spectral Range (nm)	400-1000	900-1700
Spectral Bands	224	224
Spatial Sampling (px)	1024	640
Spectral FWHM (nm)	5.5	8
Spectral Resolution (nm)	2.7	3.5

4) *Grade D:* Samples with advanced corrosion, including extensive structural damage.

In the SSC Samples dataset, the first three samples are classified as Grade A due to their pristine condition. Samples at Levels 1 and 2 are defined as Grade B. Although Level 2 samples are exposed for an additional half-hour and show more corrosion, they still exhibit superficial corrosion with intact areas. Meanwhile, Level 3 samples are classified as Grade C due to generalized corrosion (see Table III).

Similarly, the OC Samples dataset is classified (see Table IV). Samples 1, 2, and 3 are categorized as Grade A before the corrosion process began, i.e., on day 0. Subsequently, on days 7 and 14, they are classified as Grade B; although the level of corrosion increases gradually, it remains superficial and not widespread. Sample 3 m (with mill scale) is considered Grade A, and Sample 4 is assigned Grade D due to its significant deterioration.

C. Hyperspectral Measurements

Two hyperspectral Specim cameras have been employed: the FX10 and the FX17 [60], corresponding to VNIR and SWIR cameras, respectively. The main characteristics of these cameras are described in Table V. Both cameras utilize push broom technology.

The images of the samples were acquired in the laboratory using a hyperspectral imaging acquisition platform (see Fig. 5). In addition, radiometric calibration in (1) was performed using white and black references. For the

of oxide on the surface of the steel during hot rolling [see Fig. 4(a)]. In this case, Sample 3 is referred to as Sample 3 m. Finally, Sample 4 was placed on a platform in the middle of the sea for four months [see Fig. 4(b)].

B. Corrosion Severity Assessment of Metal Samples

Each metal sample is meticulously inspected and assessed, and a corrosion grade is assigned based on its condition according to the Swedish standard SIS 05 5900 [59]. This classification relies on visual appearance and structural damage observed in the samples, following predefined criteria to ensure evaluation consistency.

1) *Grade A:* Sample without signs of corrosion in pristine condition.
2) *Grade B:* Sample with superficial and scattered corrosion without significant structural damage.
3) *Grade C:* Generalized corrosion present in the sample but without the formation of deep cavities.
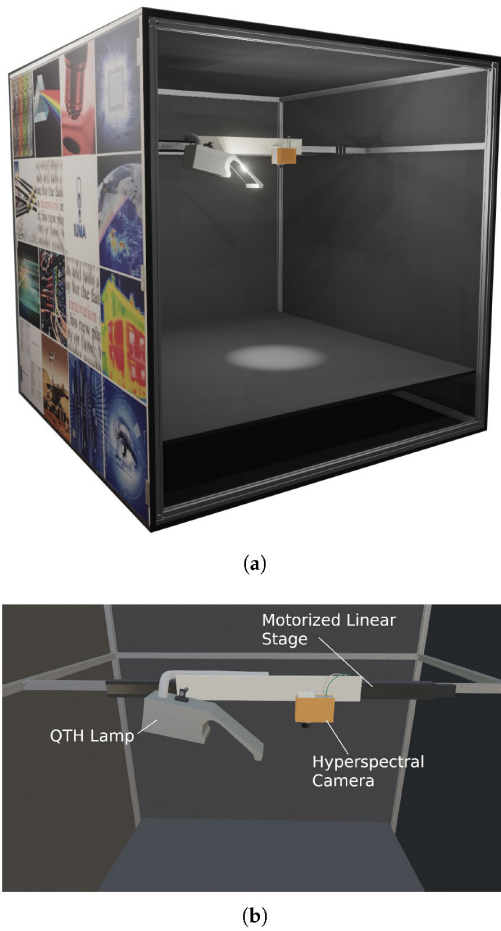
(a)

(b)

Fig. 5. Experimental setup for hyperspectral measurements [63]. (a) Three-dimensional model of the acquisition system. (b) Detailed view of the main components.

white reference, a Spectralon Diffuse Reflectance Material [61] with a reflectance of 99% was used, whereas, for the black reference, the camera lens was completely closed. Radiance, which is the measure of the amount of light reflected by the sample, was used in the calibration process. The value obtained based on (1) represents the reflectance [62], which is the calibrated value obtained from the radiance, and it ranges from 0 to 1

$$\text{Reflectance} = \frac{\text{Radiance} - \text{Dark Reference}}{\text{White Reference} - \text{Dark Reference}}. \quad (1)$$

D. Hyperspectral Image Preprocessing

In this study, the importance of analyzing the VNIR and SWIR spectral ranges together is emphasized to obtain a comprehensive and accurate spectral signature of corroded surfaces. To achieve this, we employ the scale-invariant feature transform (SIFT) algorithm, which is widely recognized for its robustness in detecting and matching key points across images with varying conditions [64], [65]. The flowchart in Fig. 6 illustrates the sequential stages of SIFT's operation from detecting scale-space extrema to generating unique descriptors for each key point. This process allows for the reliable identification of invariant features that remain stable across changes in scale, orientation, and lighting, ensuring precise
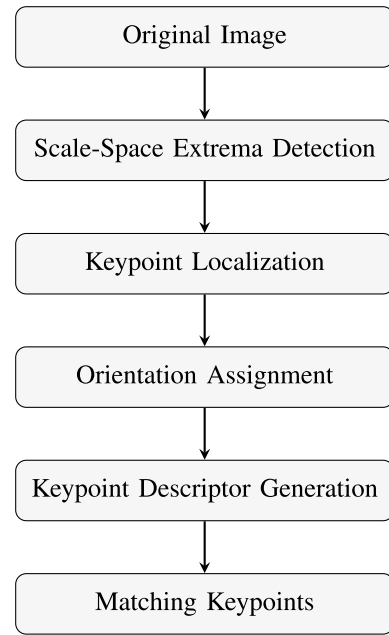

Fig. 6. Flowchart of the SIFT algorithm.

image alignment. This approach is essential for accurately registering images from different spectral bands despite challenges such as variations in brightness, scale, and similarities between features [66], [67].

To select the best matches, a geometric constraint based on the distance between matched features was applied, in addition to the random sample consensus (RANSAC) algorithm [68], [69]. This methodology was crucial in accurately aligning the images despite the challenges presented by low brightness, scale variation, and similarity between different image features.

Special emphasis was placed on selecting 2-D images for key point analysis, focusing on the bands with the highest correlation between the hyperspectral cameras used. This selection process significantly improved the results of the study, ensuring the precision and quality of the resulting spectral signature [70].

E. CI Methodology

The CSI was developed from the SSC Samples dataset. This analytical process focused on spectral ranges and specific bands that are mostly influenced by corrosion, with the aim of covering the diversity of corrosion products and identifying common patterns associated with their progression. These observations are detailed in the Section III-A.

The CSI is obtained by a mathematical calculation described in (2), which involves four spectral bands able to distinguish different levels of corrosion. Each spectral band is represented as R_center wavelength, indicating its reflectance value

$$\text{CSI} = \left(\frac{R_{790} - R_{450}}{R_{790} + R_{450}} + (R_{1340} - R_{1430}) \right) \bigg/ R_{790}. \quad (2)$$

This index allows a quantitative assessment at the pixel level of the state of corrosion, facilitating a detailed analysis of its distribution and severity in the examined area. Values close

to zero indicate the absence of corrosion, whereas higher values signify an increasing presence of corrosion. In the datasets proposed in this study, the CSI values range from zero to five, without normalization.

To determine the overall corrosion degree of the sample, the CSI values are averaged for every pixel. From this result, the plate is classified into A, B, C, or D grade. This classification provides information on the condition of the metal without the need for additional qualitative evaluations.

An optical microscope was used to evaluate areas with minimal or no visible corrosion. This technique enabled a thorough examination at the microscopic level to detect early signs of corrosion, which are not easily visible to the naked eye. Microscopic analysis was conducted on different areas of the same sample to confirm the presence of corrosion and verify corresponding CSI values in these regions.

The CSI robustness was confirmed using the OC Samples dataset, which analyzed steel and iron plates exposed to environmental and corrosion conditions. This step validated the applicability and reliability of the index in different contexts.

Finally, a comparison was carried out between the CSI and the CI. For this purpose, images from the SSC Samples dataset were used, and the methodology described in [54] was followed. To ensure a fair assessment, the CSI is normalized. This normalization facilitates an accurate and direct comparison between the indices, where a value of 0 indicates no corrosion and a value of 1, the maximum level of corrosion detected.

III. RESULTS AND DISCUSSION

A. Spectral Corrosion Characterization of Steel and Iron Samples

The formation of corrosion in steel and iron is manifested through the appearance of various corrosion products, which vary depending on the chemical reactions involved. These products' corrosion presents different colors and spectral signatures. Inspired by the approach of De Kerf et al. [45], who investigated the materials present in corroded steel plates under similar conditions to this study, within a salt spray chamber, the presence of hematite, lepidocrocite, goethite, and magnetite was highlighted. It was observed that hematite and lepidocrocite predominate in the early phases of corrosion. However, after 8 h of exposure to the saline environment, a significant increase in the presence of goethite, identified by brownish tones, as well as magnetite, which presents a black color, was noted.

The present study has identified similar patterns. To analyze spectral signatures across corrosion levels, we calculated the mean and standard deviation of signatures for each level. The full spectral results obtained are illustrated in Fig. 7.

Iron plates without corrosion show spectral signatures with an ascending and almost linear trend. When the corrosion process began, areas with yellowish tones appeared. These areas clearly present a change in the spectral signature, specifically in the visible spectrum, where the slope between 400 and 600 nm becomes steeper. In addition, a descending trend is observed starting at approximately 1200 nm.
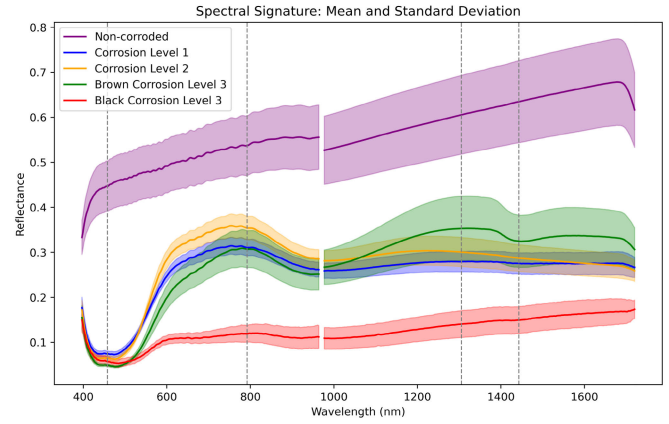

Fig. 7. Spectral signatures of steel under progressive corrosion: from pristine to advanced stages. The spectral bands employed in the spectral index are marked with dashed lines.

Samples exposed for an additional 30 min (Level 2) showed a similar color but with an increased density of corrosion. In these cases, the decay in the SWIR region was generally more abrupt compared to the initial samples.

In the samples exhibited for 24 h in the salt spray chamber, two clearly differentiated zones appear, both in color and spectral signature. One zone, with brown and dark orange tones (brown corrosion, Level 3), shows a drastic change in the SWIR region. Between 1350 and 1450 nm, there is a further decrease in reflectance, even greater than in previous observations. The black zones (black corrosion, Level 3) exhibit extremely low reflectance, practically close to zero.

The CSI employs four specific bands: 457.50, 791.91, 1305.08, and 1442.60 nm. The relationship between the normalized difference of the 457.50- and 791.91-nm bands, in the visible and near-infrared regions, enables the detection of corrosion in yellowish, orange, and brown tones, characteristics of corrosion.

In addition, the bands in the SWIR region (1305.08 and 1442.60 nm) show a more pronounced decline in reflectance as corrosion progresses, while, in noncorroded areas, there is an increase in the spectral signature. This contrast makes these bands a strong indicator of corrosion levels. When no corrosion is present, this difference tends to be negative, which is counteracted by the previous normalized value between the 457.50- and 791.91-nm bands. This balance allows the CSI to reliably indicate corrosion, with values close to zero indicating no corrosion and higher values reflecting greater corrosion levels.

In order to incorporate corrosion products defined as black corrosion, which have very low reflectance across the spectrum, the entire index is divided by the 791.91-nm band. This adjustment amplifies the response for magnetite, yielding higher values where it is present.

The correlation coefficients between the CSI and the spectral bands were calculated to evaluate the relationship between the index and the reflectance values at different wavelengths. The results of the correlation analysis are shown in Table VI. These correlations demonstrate a strong relationship between the CSI and the reflectance values at the four spectral bands, with
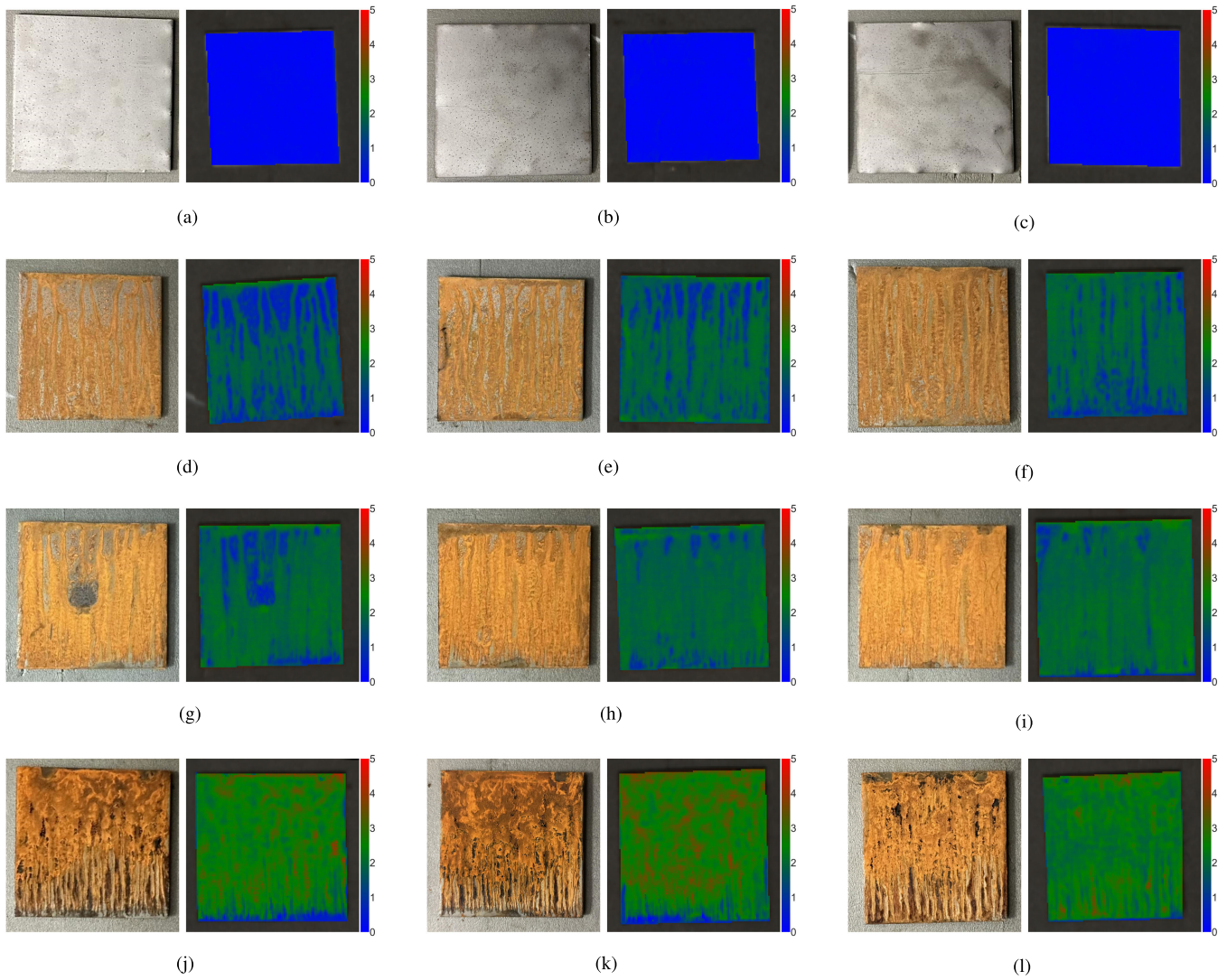
Fig. 8. RGB images and CSI color map of SSC Samples. (a) Sample 1. (b) Sample 2. (c) Sample 3. (d) Sample 4. (e) Sample 5. (f) Sample 6. (g) Sample 7. (h) Sample 8. (i) Sample 9. (j) Sample 10. (k) Sample 11. (l) Sample 12.

TABLE VI
CORRELATION COEFFICIENTS BETWEEN THE CSI AND SPECTRAL BANDS

Spectral Bands	Wavelength (nm)	Correlation Coefficient (CSI)
Band 1	457.50	-0.97
Band 2	791.91	-0.90
Band 3	1305.08	-0.86
Band 4	1442.60	-0.90

Fig. 9. Zones defined in the samples. On the left, the sample was without corrosion; on the right, the sample was exposed for 20 min in a salt spray chamber.

the strongest correlation observed for Band 1 (457.50 nm), indicating that the index accurately reflects spectral changes due to corrosion in these wavelengths.

B. Analysis of CSI

The CSI index is applied to the dataset of SSC Samples obtained with the salt spray chamber. The corrosion degree of each sample is determined by the CSI mean values ($\overline{\text{CSI}}$). Boundaries defined visually determine the corrosion degree.

1) *Grade A:* $\overline{\text{CSI}} < 1$.
2) *Grade B:* $1 \leq \overline{\text{CSI}} < 2$.
3) *Grade C:* $2 \leq \overline{\text{CSI}} < 3$.
4) *Grade D:* $\overline{\text{CSI}} \geq 3$.

CSI values are translated into colors, as shown in Fig. 8, together with the RGB image for the 11 iron samples. Table VII summarizes the mean values along with the standard deviation (σ) for each sample and details the corrosion degree.

Level 0 does not show any sign of corrosion, being the three samples correctly defined as Grade A. Level 1 samples

Fig. 10. Microscopic image of the areas defined in Fig. 9. (a) Zone 0. (b) Zone 1. (c) Zone 2. (d) Zone 3.
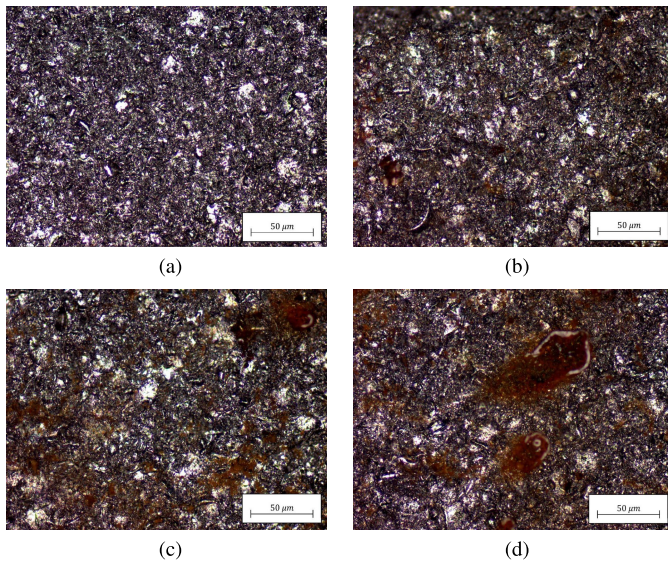
TABLE VII
RESULTS OF SSC SAMPLES

SSC Samples	$\overline{CSI} \pm \sigma$	Corrosion Degree
Sample 1	0.12 ± 0.07	Grade A
Sample 2	0.12 ± 0.08	Grade A
Sample 3	0.11 ± 0.05	Grade A
Sample 4	1.46 ± 0.42	Grade B
Sample 5	1.71 ± 0.34	Grade B
Sample 6	1.73 ± 0.31	Grade B
Sample 7	1.80 ± 0.36	Grade B
Sample 8	1.85 ± 0.23	Grade B
Sample 9	1.93 ± 0.26	Grade B
Sample 10	2.45 ± 0.50	Grade C
Sample 11	2.62 ± 0.54	Grade C
Sample 12	2.30 ± 0.34	Grade C

present a color map in accordance with the visual appearance, and therefore, these samples are classified as Grade B due to the increase of the average CSI.

Level 2 shows similar results to Level 1, with a slight increase in the average CSI due to the higher exposure in the saline environment. Finally, at Level 3, the color map begins to reveal areas of increased corrosion represented in red, correctly classifying the samples as Grade C. The spectral index identifies the different corrosion products, from black to orange corrosion. Some areas at the bottom of Samples 10, 11, and 12 that do not present corrosion are correctly recognized.

C. Early-Stage Corrosion

To analyze early-stage corrosion, a corrosion-free sample was studied together with another sample exposed for 20 min in a salt spray chamber under the same conditions as the SSC Samples. Study zones were defined on both samples, as shown in Fig. 9. Zone 0 represents an uncorroded sample; Zone 1 corresponds to an area that, although exposed to the saline mist chamber, appears corrosion-free; Zone 2 shows very subtle signs of corrosion, practically invisible to the naked eye; and finally, Zone 3 exhibits slight visible corrosion. Applying the CSI to these zones, as shown in Table VIII,

TABLE VIII
CSI VALUES IN ZONES DEFINED IN FIG. 9

Zones	$\overline{CSI} \pm \sigma$
Zone 0	0.11 ± 0.02
Zone 1	0.21 ± 0.02
Zone 2	0.4 ± 0.1
Zone 3	0.5 ± 0.2

revealed a progressive increase in CSI values, suggesting that CSI effectively enables early corrosion detection.

To validate this observation, these zones were examined under an optical microscope. The images illustrate how the surface in Zone 0 remains completely corrosion-free [see Fig. 10(a)], while initial signs of corrosion appear in Zone 1 [see Fig. 10(b)]. In Zone 2, corrosion is more pronounced [see Fig. 10(c)], and in Zone 3, it is clearly visible [see Fig. 10(d)], confirming the utility of CSI for early-stage corrosion detection.

D. Robustness of CSI

To assess the CSI robustness, the second dataset OC Samples are evaluated. Fig. 11 illustrates the deterioration of the samples over two weeks. Samples 2 and 3 show significant corrosion in the lower half areas exposed to seawater compared to Sample 1, which was only exposed to outdoor environmental conditions. However, the protected areas of Samples 2 and 3 (upper half area) remained in better condition than Sample 1. In particular, Sample 3 suffers from corrosion at the edges of the protected area due to accidental seawater infiltration.

Table IX shows a progressive increase in $\overline{CSI}$ for Samples 1, 2, and 3 over time. In Sample 1, the CSI rose by approximately one unit during the first week and then more moderately in the second week, with an increase of around 0.3 units. This pattern suggests an expected slowdown in the corrosion process: initially, corrosion is more intense, but it later stabilizes and slows down. In addition, the standard deviation in Sample 1 is close to zero, confirming uniform corrosion across the sample due to its consistent exposure.

For Samples 2 and 3, although there was also an increase of one unit in the first week and 0.3 units in the second, the corrosion distribution differed. The protected section of these samples remained corrosion-free, while the section exposed to saltwater experienced more intense corrosion than Sample 1 due to the harsher exposure conditions. This variability between the exposed and protected sections is reflected in the standard deviation, which is close to one in these cases.

Each sample was accurately categorized based on the CSI readings collected over multiple days, with only a minor discrepancy noted for Sample 2 on Day 7. In this particular case, the difference between the protected and exposed sections caused a slight misclassification; the corroded section showed a low corrosion level, resulting in an average CSI of less than one. This outcome aligns with expectations, as one-half of the sample was purposefully exposed to corrosion, while the other was shielded. Despite this, the overall CSI remained close to one, and the higher standard deviation
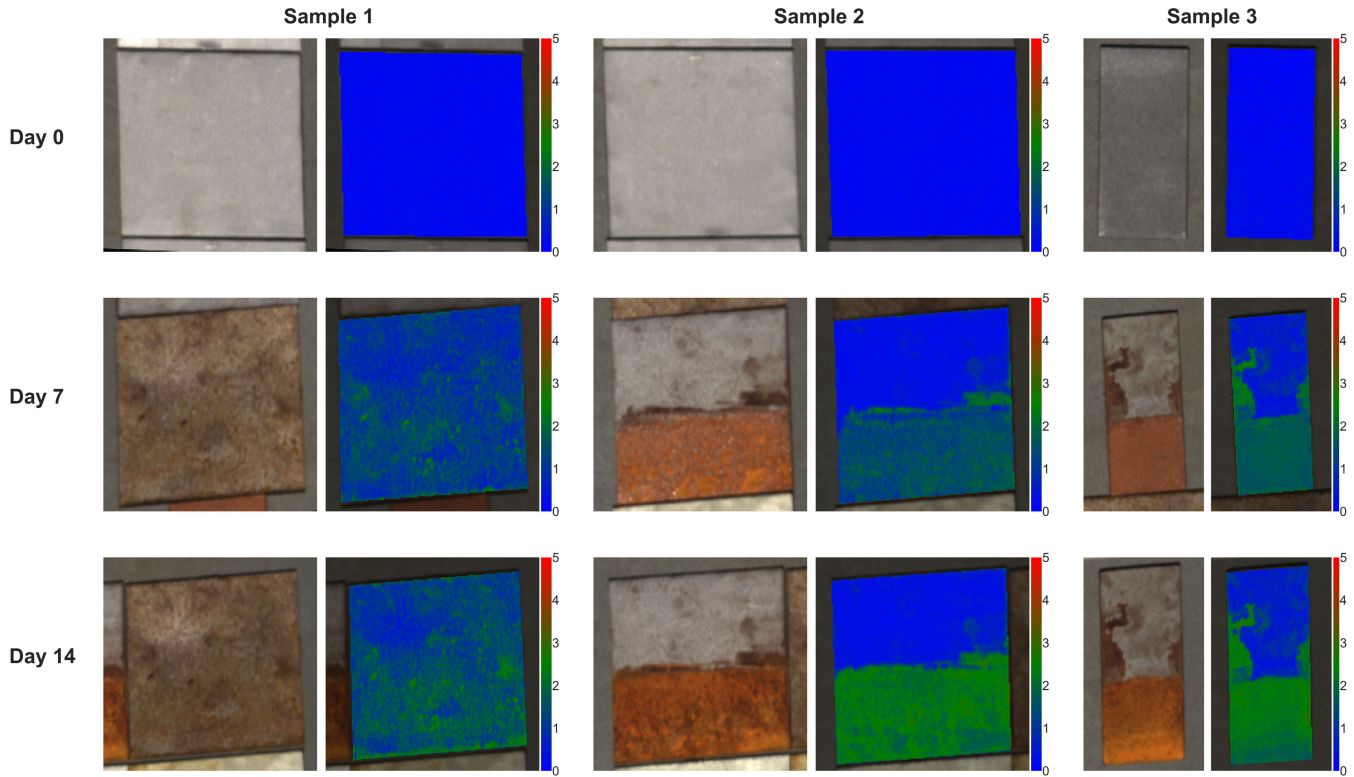
Fig. 11.   RGB images and CSI color map of OC Samples.

effectively reflected the corrosion variation between the two halves, highlighting the spectral index's sensitivity to such environmental differences.

Sample 3 m was accurately classified as noncorrosive, despite exhibiting a different spectral signature and visual appearance attributable to the oxide layer produced by hot rolling, known as mill scale [see Fig. 12(a)]. Sample 4 showed advanced deterioration and was classified as Grade D [see Fig. 12(b)]. Although small areas on the right-hand side of the plate appeared to be free of corrosion, the exact nature of these areas requires further chemical analysis for precise determination.

While the CSI has proven effective in detecting a range of corrosion products commonly observed under saline conditions, its performance may vary with corrosion products formed under different environmental factors. The robustness of the CSI has been studied with various types of steel and iron under coastal environments, where the primary corrosive agent is the salinity of seawater. For this reason, the index includes four specific bands designed to encompass corrosion products typical of these conditions. Outside this context, the spectral index may present limitations.

E. CSI Versus CI: A Comparative Analysis

For the comparative analysis, Samples 1, 4, 7, and 10 were selected from the SSC Samples dataset to study one representative sample from each level.

The CSI values were normalized, with a maximum value of 4.5 and a minimum value of 0.
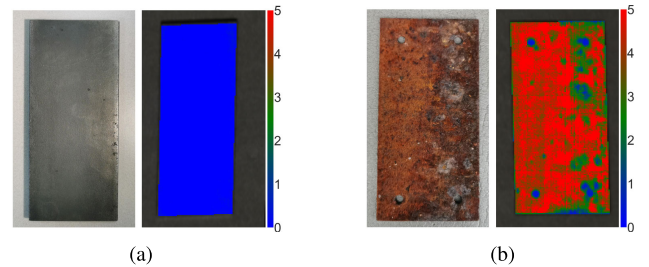

(a)   (b)

Fig. 12.   RGB images and CSI color map of OC Samples. (a) Sample 3 m. (b) Sample 4.

TABLE IX
RESULTS OF OC SAMPLES

OC Samples	Day	$\overline{\text{CSI}} \pm \sigma$	Grade
Samples 1	Day 0	0.16 ± 0.04	Grade A
	Day 7	1.15 ± 0.29	Grade B
	Day 14	1.44 ± 0.37	Grade B
Samples 2	Day 0	0.16 ± 0.04	Grade A
	Day 7	0.92 ± 0.60	Grade A
	Day 14	1.36 ± 0.94	Grade B
Samples 3	Day 0	0.18 ± 0.08	Grade A
	Day 7	1.22 ± 0.61	Grade B
	Day 14	1.52 ± 0.78	Grade B
Samples 3m	-	-0.16 ± 0.13	Grade A
Samples 4	Day 210	4.12 ± 1.09	Grade D

For the CI, a reference representative of advanced corrosion in the analyzed metal was established. This reference covers a range between 500 and 600 nm. The calibration parameters used to adjust the values were visually determined. This procedure is defined as specified in [54].
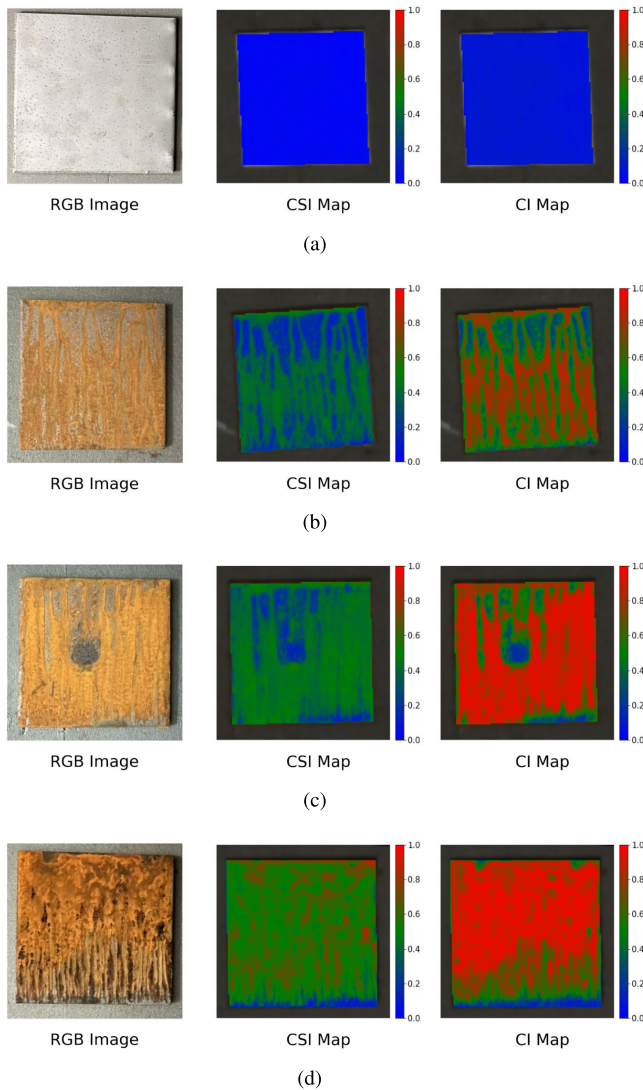
Fig. 13. RGB image, CSI color map, and CI color map, respectively. (a) Sample 1. (b) Sample 4. (c) Sample 7. (d) Sample 10.

TABLE X
COMPARISON OF CSI VERSUS CI VALUES

SSC Samples	$\overline{\text{CSI}} \pm \sigma$	$\overline{\text{CI}} \pm \sigma$
Sample 1	0.03 ± 0.02	0.08 ± 0.01
Sample 4	0.32 ± 0.09	0.62 ± 0.18
Sample 7	0.40 ± 0.08	0.79 ± 0.19
Sample 10	0.54 ± 0.11	0.79 ± 0.20

complexity and enables rapid analysis. In addition, the CSI calculation relies on simple arithmetic operations, making it computationally less intensive compared to more complex formulas, such as the ACD. ACD involves trigonometric functions and vector norms, which increase computational cost and processing time. This efficiency makes CSI particularly advantageous for deployment in multispectral cameras, where speed and cost are critical factors, especially in applications like field inspections, industrial monitoring, and any other application where real time is mandatory.

A key distinction between the CI and CSI indices is their dependence on reference values. CI requires specific reference values that vary according to the type of steel or iron alloy, complicating its application across different materials and limiting its versatility. In contrast, CSI consistently provides accurate results across various iron and steel alloys without needing material-specific reference values. This characteristic makes CSI a more straightforward and flexible tool for corrosion assessment, allowing reliable application across a range of alloy compositions without sacrificing precision.

IV. CONCLUSION

The CSI has established itself as a revolutionary technique in the detection and quantification of corrosion in steel and iron materials, especially highlighting its ability to automate corrosion monitoring in coastal environments. Using VNIR and SWIR spectra analysis in both controlled and uncontrolled conditions, the CSI has proven to be superior to the CI as it uses a formula that integrates only four spectral bands. In addition, it does not require references or pre-established parameters for each type of metal studied. Another point to highlight is the ease with which it allows for the identification of a wider range of corrosion products and provides an accurate measurement of metal deterioration.

This study emphasizes the ability of CSI to be integrated into multispectral sensor systems, thus extending its applicability from the laboratory to industrial and natural environments. Avoiding the use of push broom HSI systems not only reduces costs but also overcomes the limitations associated with these technologies, which are developed primarily for laboratory applications and are restricted for their use in the field. The use of multispectral sensors equipped with snapshot technology, capable of capturing spectral information in a specific range of wavelengths, can offer an optimal balance between ease of use and accuracy.

These advances promise not only to optimize preventive maintenance strategies but also to mark a significant evolution in corrosion monitoring technologies. Providing infrastructure maintenance and promoting a more efficient and sustainable management of resources. In addition, the CSI has demonstrated the capability to detect early-stage corrosion, offering

The color maps for CSI and CI are shown in Fig. 13. CI effectively differentiates between corroded and noncorroded areas but lacks sensitivity to variations in corrosion severity. CI primarily depends on spectral slopes between 500 and 600 nm, which limits its ability to distinguish more advanced degradation levels. As shown in Table X, Samples 7 and 10 share similar CI values, with Sample 4 showing a close value, indicating reduced sensitivity, especially to dark corrosion products.

In contrast, CSI exhibits a more gradual response across different corrosion levels, with a steady increase in $\overline{\text{CSI}}$ values from Sample 1 to Sample 10, as shown in Table X. This trend suggests that CSI is more responsive to varying corrosion stages, including advanced ones with dark-toned corrosion products, thereby offering a finer resolution and more accurate assessment of corrosion severity.

The CSI also offers practical advantages by simplifying the analysis process. Unlike CI, which requires a continuous spectral range for accurate measurements, CSI is based on only four specific wavelengths, which reduces the computational

an essential advantage for proactive maintenance and extending asset life. This study has developed the CSI for coastal environments; however, future research could investigate the behavior of the CSI under other environmental conditions, where different corrosion products may emerge. Such research would provide a more comprehensive view of the limitations and versatility of the index.

ACKNOWLEDGMENT

REFERENCES

[1] B. Valdez, J. Ramirez, A. Eliezer, M. Schorr, R. Ramos, and R. Salinas, "Corrosion assessment of infrastructure assets in coastal seas," *J. Mar. Eng. Technol.*, vol. 15, no. 3, pp. 124–134, Sep. 2016, doi: 10.1080/20464177.2016.1247635.

[2] M. G. Fontana and N. D. Greene, *Corrosion Engineering*, 2nd ed., New York, NY, USA: McGraw-Hill, 1967.

[3] S. Caines, F. Khan, and J. Shirokoff, "Analysis of pitting corrosion on steel under insulation in marine environments," *J. Loss Prevention Process Industries*, vol. 26, no. 6, pp. 1466–1483, Nov. 2013. [Online]. Available: https://www.sciencedirect.com/science/article/pii/S0950423013001873

[4] F. W. Schremp, "Corrosion prevention for offshore platforms," *J. Petroleum Technol.*, vol. 36, no. 4, pp. 605–612, Apr. 1984, doi: 10.2118/9986-pa.

[5] C. G. Soares, Y. Garbatov, A. Zayed, and G. Wang, "Influence of environmental factors on corrosion of ship structures in marine atmosphere," *Corrosion Sci.*, vol. 51, no. 9, pp. 2014–2026, Sep. 2009. [Online]. Available: https://www.sciencedirect.com/science/article/pii/S0010938X09002315

[6] H. Son, N. Hwang, C. Kim, and C. Kim, "Rapid and automated determination of rusted surface areas of a steel bridge for robotic maintenance systems," *Autom. Construct.*, vol. 42, pp. 13–24, Jun. 2014. [Online]. Available: https://www.sciencedirect.com/science/article/pii/S0926580514000417

[7] *Corrosion Detection and Monitoring—A Review*, NACE Int., Houston, TX, USA, 2000.

[8] A. Zaki, H. Chai, D. Aggelis, and N. Alver, "Non-destructive evaluation for corrosion monitoring in concrete: A review and capability of acoustic emission technique," *Sensors*, vol. 15, no. 8, pp. 19069–19101, Aug. 2015. [Online]. Available: https://www.mdpi.com/1424-8220/15/8/19069

[9] D. W. Brown, R. J. Connolly, M. Garvan, H. Li, V. S. Agarwala, and G. Vachtsevanos, "A novel linear polarization resistance corrosion sensing methodology for aircraft structure," in *Proc. Annu. Conf. PHM Soc.*, Sep. 2014, vol. 6, no. 1.

[10] W. Zhu, J. L. Rose, J. N. Barshinger, and V. S. Agarwala, "Ultrasonic guided wave NDT for hidden corrosion detection," *Res. Nondestruct. Eval.*, vol. 10, no. 4, pp. 205–225, 1998, doi: 10.1080/09349849809409629.

[11] M. Á. Climent, M. Miró, J. Carbajo, P. Poveda, G. de Vera, and J. Ramis, "Use of non-linear ultrasonic techniques to detect cracks due to steel corrosion in reinforced concrete structures," *Materials*, vol. 12, no. 5, p. 813, Mar. 2019. [Online]. Available: https://www.mdpi.com/1996-1944/12/5/813

[12] H. Song, Q. Xiao, G. Wang, J. Zhang, and W. Hu, "A composite approach of electromagnetic acoustic transducer and eddy current for inner and outer corrosion defects detection," *IEEE Trans. Instrum. Meas.*, vol. 72, pp. 1–11, 2023.

[13] S. Li, Y.-G. Kim, S. Jung, H.-S. Song, and S.-M. Lee, "Application of steel thin film electrical resistance sensor for in situ corrosion monitoring," *Sens. Actuators B, Chem.*, vol. 120, no. 2, pp. 368–377, Jan. 2007. [Online]. Available: https://www.sciencedirect.com/science/article/pii/S0925400506001328

[14] C. Jimenez-Marcos, J. C. Mirza-Rosca, M. S. Baltatu, and P. Vizureanu, "Experimental research on new developed titanium alloys for biomedical applications," *Bioengineering*, vol. 9, no. 11, p. 686, Nov. 2022. [Online]. Available: https://www.mdpi.com/2306-5354/9/11/686

[15] J. Cabrera-Peña, S. J. Brito-Garcia, J. C. Mirza-Rosca, and G. M. Callico, "Electrical equivalent circuit model prediction of high-entropy alloy behavior in aggressive media," *Metals*, vol. 13, no. 7, p. 1204, Jun. 2023. [Online]. Available: https://www.mdpi.com/2075-4701/13/7/1204

[16] Y. Zou, J. Wang, and Y. Y. Zheng, "Electrochemical techniques for determining corrosion rate of rusted steel in seawater," *Corrosion Sci.*, vol. 53, no. 1, pp. 208–216, Jan. 2011. [Online]. Available: https://www.sciencedirect.com/science/article/pii/S0010938X10004427

[17] M. S. B. Reddy et al., "Sensors in advancing the capabilities of corrosion detection: A review," *Sens. Actuators A, Phys.*, vol. 332, Dec. 2021, Art. no. 113086.

[18] M. Veneranda, J. Aramendia, L. Bellot-Gurlet, P. Colomban, K. Castro, and J. M. Madariaga, "FTIR spectroscopic semi-quantification of iron phases: A new method to evaluate the protection ability index (PAI) of archaeological artefacts corrosion systems," *Corrosion Sci.*, vol. 133, pp. 68–77, Apr. 2018.

[19] H. Namduri and S. Nasrazadani, "Quantitative analysis of iron oxides using Fourier transform infrared spectrophotometry," *Corrosion Sci.*, vol. 50, no. 9, pp. 2493–2497, Sep. 2008.

[20] J. P. Labbé, J. Lédion, and F. Hui, "Infrared spectrometry for solid phase analysis: Corrosion rusts," *Corrosion Sci.*, vol. 50, no. 5, pp. 1228–1234, May 2008.

[21] R. J. Thibeau, C. W. Brown, and R. H. Heidersbach, "Raman spectra of possible corrosion products of iron," *Appl. Spectrosc.*, vol. 32, no. 6, pp. 532–535, Nov. 1978, doi: 10.1366/000370278774330739.

[22] K. Asami and K. Hashimoto, "X-ray photoelectron spectroscopy for corrosion studies," *Langmuir*, vol. 3, no. 6, pp. 897–904, Nov. 1987, doi: 10.1021/la00078a005.

[23] H. Kerdoncuff, W.-I. Lin, and L. J. Wacker, "Spectroscopic techniques for corrosio N detection using drones," Danish Nat. Metrol. Inst. (DFM), Kongens Lyngby, Denmark, Tech. Rep. DFM-2017-R005, 2017.

[24] F. N. S. Medeiros, G. L. B. Ramalho, M. P. Bento, and L. C. L. Medeiros, "On the evaluation of texture and color features for nondestructive corrosion detection," *EURASIP J. Adv. Signal Process.*, vol. 2010, no. 1, pp. 1–7, Dec. 2010.

[25] K.-W. Liao and Y.-T. Lee, "Detection of rust defects on steel bridge coatings via digital image recognition," *Autom. Construct.*, vol. 71, pp. 294–306, Nov. 2016. [Online]. Available: https://www.sciencedirect.com/science/article/pii/S0926580516301625

[26] M. Khayatazad, L. De Pue, and W. De Waele, "Detection of corrosion on steel structures using automated image processing," *Develop. Built Environ.*, vol. 3, Aug. 2020, Art. no. 100022.

[27] A. Rahman, Z. Y. Wu, and R. Kalfarisi, "Semantic deep learning integrated with RGB feature-based rule optimization for facility surface corrosion detection and evaluation," *J. Comput. Civil Eng.*, vol. 35, no. 6, Nov. 2021, Art. no. 04021018.

[28] D. N. Lavadiya, H. U. Sajid, R. K. Yellavajjala, and X. Sun, "Hyperspectral imaging for the elimination of visual ambiguity in corrosion detection and identification of corrosion sources," *Struct. Health Monitor.*, vol. 21, no. 4, pp. 1678–1693, Jul. 2022, doi: 10.1177/14759217211041690.

[29] S. F. Di Gennaro, P. Toscano, M. Gatti, S. Poni, A. Berton, and A. Matese, "Spectral comparison of UAV-based hyper and multispectral cameras for precision viticulture," *Remote Sens.*, vol. 14, no. 3, p. 449, Jan. 2022. [Online]. Available: https://www.mdpi.com/2072-4292/14/3/449

[30] J. Qin, K. Chao, M. S. Kim, R. Lu, and T. F. Burks, "Hyperspectral and multispectral imaging for evaluating food safety and quality," *J. Food Eng.*, vol. 118, no. 2, pp. 157–171, Sep. 2013. [Online]. Available: https://www.sciencedirect.com/science/article/pii/S0260877413001659

[31] J. M. Bioucas-Dias, A. Plaza, G. Camps-Valls, P. Scheunders, N. Nasrabadi, and J. Chanussot, "Hyperspectral remote sensing data analysis and future challenges," *IEEE Geosci. Remote Sens. Mag.*, vol. 1, no. 2, pp. 6–36, Jun. 2013.

[32] M. Borengasser, W. S. Hungate, and R. Watkins, *Hyperspectral Remote Sensing: Principles and Applications*. Boca Raton, FL, USA: CRC Press, 2007.

[33] A. S. Laliberte, M. A. Goforth, C. M. Steele, and A. Rango, "Multispectral remote sensing from unmanned aircraft: Image processing workflows and applications for rangeland environments," *Remote Sens.*, vol. 3, no. 11, pp. 2529–2551, Nov. 2011.

[34] M. Halicek, H. Fabelo, S. Ortega, G. M. Callico, and B. Fei, "In-vivo and ex-vivo tissue analysis through hyperspectral imaging techniques: Revealing the invisible features of cancer," *Cancers*, vol. 11, no. 6, p. 756, May 2019. [Online]. Available: https://www.mdpi.com/2072-6694/11/6/756

[35] R. Leon et al., "Non-invasive skin cancer diagnosis using hyperspectral imaging for in-situ clinical support," *J. Clin. Med.*, vol. 9, no. 6, p. 1662, Jun. 2020. [Online]. Available: https://www.mdpi.com/2077-0383/9/6/1662

[36] Y.-Z. Feng and D.-W. Sun, "Application of hyperspectral imaging in food safety inspection and control: A review," *Crit. Rev. Food Sci. Nutrition*, vol. 52, no. 11, pp. 1039–1058, Nov. 2012.

[37] P. Horstrand, R. Guerra, A. Rodriguez, M. Diaz, S. Lopez, and J. F. Lopez, "A UAV platform based on a hyperspectral sensor for image capturing and on-board processing," *IEEE Access*, vol. 7, pp. 66919–66938, 2019.

[38] R. Guerra et al., "Optimal UAV movement control for farming area scanning using hyperspectral pushbroom sensors," in *Proc. 34th Conf. Design Circuits Integr. Syst. (DCIS)*, Nov. 2019, pp. 1–6.

[39] E. Simova and P. A. Rochefort, "Active spectral imaging nondestructive evaluation (SINDE) camera," *CNL Nucl. Rev.*, vol. 5, no. 1, pp. 121–125, Jun. 2016.

[40] W. G. Rowley, "Hyperspectral imaging for detection of corrosion on intermediate level nuclear waste containers," Doctoral dissertation, School Metallurgy Mater., Univ. Birmingham, Birmingham, U.K., 2019.

[41] E. Catelli, L. L. Randeberg, H. Strandberg, B. K. Alsberg, A. Maris, and L. Vikki, "Can hyperspectral imaging be used to map corrosion products on outdoor bronze sculptures?" Norwegian Univ. Sci. Technol. (NTNU), Trondheim, Norway, Tech. Rep., 2018.

[42] M. M. Antony, C. Sandeep, and M. V. Matham, "High resolution probe for corrosion monitoring using hyper spectral imaging," in *Proc. AIP Conf.*, 2021, vol. 2317, no. 1.

[43] M. M. Antony, C. S. S. Sandeep, H. Lim, and M. V. Matham, "Hyperspectral vision based probe for in situ corrosion monitoring in saline environments," *IEEE Trans. Instrum. Meas.*, vol. 71, pp. 1–7, 2022.

[44] T. De Kerf, A. Gestels, K. Janssens, P. Scheunders, G. Steenackers, and S. Vanlanduit, "Quantitative detection of corrosion minerals in carbon steel using shortwave infrared hyperspectral imaging," *RSC Adv.*, vol. 12, no. 50, pp. 32775–32783, 2022.

[45] T. De Kerf, G. Pipintakos, Z. Zahiri, S. Vanlanduit, and P. Scheunders, "Identification of corrosion minerals using shortwave infrared hyperspectral imaging," *Sensors*, vol. 22, no. 1, p. 407, Jan. 2022.

[46] P. Ma, L. Fan, and G. Chen, "Hyperspectral reflectance for determination of steel rebar corrosion and Cl^- concentration," *Construct. Building Mater.*, vol. 368, Mar. 2023, Art. no. 130506.

[47] N. Pettorelli, *The Normalized Difference Vegetation Index*. London, U.K.: Oxford Univ. Press, 2013.

[48] P. Sibandze, P. Mhangara, and J. Odindi, "A comparison of normalised difference snow index (NDSI) and normalised difference principal component snow index (NDPCSI) techniques in distinguishing snow," *South Afr. J. Geomatics*, vol. 3, no. 1, pp. 48–55, 2014.

[49] A. Bannari, D. Morin, F. Bonn, and A. R. Huete, "A review of vegetation indices," *Remote Sens. Rev.*, vol. 13, nos. 1–2, pp. 95–120, Aug. 1995.

[50] J. Xue and B. Su, "Significant remote sensing vegetation indices: A review of developments and applications," *J. Sensors*, vol. 2017, pp. 1–17, Jan. 2017.

[51] A.-K. Mahlein et al., "Development of spectral indices for detecting and identifying plant diseases," *Remote Sens. Environ.*, vol. 128, pp. 21–30, Jan. 2013.

[52] K. Mallick, B. K. Bhattacharya, and N. K. Patel, "Estimating volumetric surface moisture content for cropped soils using a soil wetness index based on surface temperature and NDVI," *Agricult. Forest Meteorol.*, vol. 149, no. 8, pp. 1327–1342, Aug. 2009.

[53] Á. Pérez-García, P. Horstrand, and J. F. López, "Ndoi, a novel oil spectral index: Comparisons and results," in *Proc. 12th Workshop Hyperspectral Imag. Signal Process., Evol. Remote Sens. (WHISPERS)*, Sep. 2022, pp. 1–5.

[54] J. Zabalza et al., "Hyperspectral imaging based corrosion detection in nuclear packages," *IEEE Sensors J.*, vol. 23, no. 21, pp. 25607–25617, Nov. 2023.

[55] J. Foreman, "Cosine distance, cosine similarity, angular cosine distance, angular cosine similarity," Nat. Inst. Standards Technol. (NIST), Gaithersburg, MD, USA, Tech. Rep., 2014.

[56] Oxford Instruments. (2013). *X-MET7000 Series Handheld XRF Analysers*. [Online]. Available: https://www.bergeng.com/mm5/downloads/oxford/X-MET-General-Brochure-Nov2013.pdf

[57] L. MatWeb. (2024). *AISI 1020 Steel, Cold Rolled*. Accessed: Jun. 10, 2024. [Online]. Available: https://www.matweb.com/search/DataSheet.aspx?MatGUID=b58ee61a3745453a9232f7864abba74f

[58] L. MatWeb. (2024). *ASTM A514 Alloy Steel Plate*. Accessed: Jun. 10, 2024. [Online]. Available: https://www.matweb.com/search/DataSheet.aspx?MatGUID=e4faa7b4b78745bd861741a3154e9e8e

[59] *SIS 05 5900: Standard for the Preparation of Steel Surfaces*. Swedish Standards Institute. Accessed: Jun. 21, 2024. [Online]. Available: https://www.utp.edu.co/cms-utp/data/bin/UTP/web/uploads/media/contratacion/documentos/granallado-normas-preparacion-de-superficie.pdf

[60] Specim Spectral Imaging. *FX Series Hyperspectral Cameras*. Accessed: Oct. 6, 2019. [Online]. Available: http://www.specim.fi/fx/

[61] SphereOptics. *Zenith Polymer Diffusers*. Accessed: Oct. 6, 2019. [Online]. Available: https://sphereoptics.de/en/product/zenith-polymer-diffusers/?c=79

[62] C. Oppenheimer, "CAMPBELL, J. B. 1997. Introduction to remote sensing, 2nd ed. Xxix + 622, pp. London, Bristol (PA): Taylor & Francis. Price $19.95 (paperback). ISBN 0 7484 0663 8," *Geological Mag.*, vol. 134, no. 6, pp. 877–883, Nov. 1997.

[63] A. Morales et al., "Laboratory hyperspectral image acquisition system setup and validation," *Sensors*, vol. 22, no. 6, p. 2159, Mar. 2022. [Online]. Available: https://www.mdpi.com/1424-8220/22/6/2159

[64] J. Wu, Z. Cui, V. S. Sheng, P. Zhao, D. Su, and S. Gong, "A comparative study of SIFT and its variants," *Meas. Sci. Rev.*, vol. 13, no. 3, pp. 122–131, Jun. 2013.

[65] OpenCV. (2023). *Introduction To SIFT (Scale-Invariant Feature Transform)*. [Online]. Available: https://docs.opencv.org/4.x/da/df5/tutorial_py_sift_intro.html

[66] S. A. K. Tareen and Z. Saleem, "Un análisis comparativo de sift, surf, kaze, akaze, orb y brisk," in *Proc. Conferencia Internacional Sobre Tecnologías de Computación, Matemáticas e Ingeniería (iCoMET)*, 2018, pp. 1–10.

[67] A. Koz, A. Çaliskan, and A. A. Alatan, "Registration of MWIR-LWIR band hyperspectral images," in *Proc. 8th Workshop Hyperspectral Image Signal Process., Evol. Remote Sens. (WHISPERS)*, Aug. 2016, pp. 1–2.

[68] J. Joglekar, S. S. Gedam, and B. Krishna Mohan, "Image matching using SIFT features and relaxation labeling technique—A constraint initializing method for dense stereo matching," *IEEE Trans. Geosci. Remote Sens.*, vol. 52, no. 9, pp. 5643–5652, Sep. 2014.

[69] Z. Hossein-Nejad and M. Nasri, "An adaptive image registration method based on SIFT features and RANSAC transform," *Comput. Electr. Eng.*, vol. 62, pp. 524–537, Aug. 2016.

[70] F. Grillini, J.-B. Thomas, and S. George, "Hyperspectral VNIR—SWIR image registration: Do not throw away those overlapping low SNR bands," in *Proc. 12th Workshop Hyperspectral Imag. Signal Process., Evol. Remote Sens. (WHISPERS)*, Sep. 2022, pp. 1–5.

Emma Hernández-Suárez was born in Las Palmas de Gran Canaria, Spain, in 1997. She received the bachelor's degree in industrial and automatic electronic engineering from the University of Las Palmas de Gran Canaria (ULPGC), Las Palmas de Gran Canaria, in 2020, and the master's degree in control and robotics from the Polytechnic University of Madrid (UPM), Madrid, Spain, in 2021. She is currently pursuing the Ph.D. degree in telecommunications technologies with ULPGC.

In 2023, she conducted a research stay in thermographic image processing at the University of Oviedo, Oviedo, Spain. He is currently a Researcher with the Institute of Applied Microelectronics, IUMA, University of Las Palmas de Gran Canaria. Her research interests include image processing, uncrewed aerial vehicles (UAVs), hyperspectral technology, thermography technologies, and their applications.
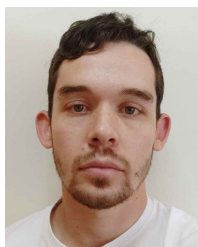
Adrián Rodríguez-Molina was born in Las Palmas de Gran Canaria, Spain, in 1998. He received the degree in industrial electronics and automatic engineering from the University of Las Palmas de Gran Canaria, Las Palmas de Gran Canaria, Spain, in 2020, and the master's degree in applied electronics and telecommunications from the Institute for Applied Microelectronics, University of Las Palmas de Gran Canaria, in 2021, where he is currently pursuing the Ph.D. degree in telecommunication technologies and computational engineering, developing a multipurpose multispectral camera with built-in artificial intelligence.

Julia Mirza-Rosca has been a Full Professor with the University of Las Palmas de Gran Canaria, Las Palmas de Gran Canaria, Spain, since 1995, and also an Honorary Professor with the Transilvania University of Brasov, Braşov, Romania. She is the Head of the Nanomaterials and Corrosion Research Group (NanCorr) and the Director of IPCC (Research and Protection in Corrosion—Canarias) from the Mechanical Engineering Department, Las Palmas de Gran Canaria University. She collaborates with the Federal Institute of Materials Research and Testing, Berlin, Germany, and the Rensselaer Polytechnic Institute, Troy, NY, USA. Her scientific interests cover, mainly, the field of electrochemical processes, corrosion, and biomaterials and nanomaterials. She specializes in the corrosion of stainless steel, titanium and its alloys, dental materials, and high-entropy alloys. She has published more than 120 articles, and for her job, she was awarded the collective prize "Ilie Murgulescu" of the Romanian Academy of Science, the prize for the best directed End-of-Degree Project, and American Medal of Honor for work carried out in the field of biomaterials.

Ámbar Pérez-García (Student Member, IEEE) was born in Las Palmas de Gran Canaria, Spain, in 1997. She received the B.Sc. degree in physics from the University of La Laguna (ULL), San Cristóbal de La Laguna, Spain, in 2019, the M.Sc. degree in remote sensing from the University of Valencia (UV), Valencia, Spain, in 2020, and the M.Sc. degree in education from the University of La Rioja (UNIR), La Rioja, Spain, in 2021. She is currently pursuing the Ph.D. degree in telecommunications technologies with the University of Las Palmas de Gran Canaria (ULPGC), Las Palmas de Gran Canaria.

In 2023, she did a research stay on neural network segmentation at HYPERCOMP, University of Extremadura, Badajoz, Spain. She was with HWM, Wageningen University and Research, Wageningen, The Netherlands, spectrally characterizing plastics. He is currently with the Institute for Applied Microelectronics, IUMA, ULPGC. Her research interests include remote sensing, hyperspectral image processing, artificial intelligence, and the detection of marine litter.

Jose López received the M.S. degree in physics (specializing in electronics) from the University of Seville, Seville, Spain, in 1989, and the Ph.D. degree from the University of Las Palmas de Gran Canaria (ULPGC), Las Palmas de Gran Canaria, Spain, in 1994.

He was with Thomson Composants Microondes, Orsay, France, in 1992. In 1995, he was with the Center for Broadband Telecommunications, Technical University of Denmark (DTU), Lyngby, Denmark. In 1996, 1997, 1999, and 2000, he was a Visiting Researcher with the Edith Cowan University (ECU), Perth, WA, Australia. He has conducted investigations at the Institute for Applied Microelectronics (IUMA), where he acted as the Deputy Director from 2009 to 2019. He is currently a Full Professor with the Department of Electronics, ULPGC. He has authored/co-authored around 150 papers in national and international journals and conferences. His current research interests include image processing, UAVs, hyperspectral technology, and their applications.

Dr. López has been actively enrolled in more than 50 research projects funded by European Community, Spanish Government, and international private industries in Europe, the United States, and Australia. He was awarded by ULPGC for his research in the field of high-speed integrated systems.